Computer-Aided Design 198 (2026) 104108

Contents lists available at ScienceDirect

Computer-Aided Design

journal homepage: www.elsevier.com/locate/cad

Extended r-adaptive isogeometric analysis for weak-discontinuous problems☆

Jingyi Cao [a,c], Ye Ji [b,*], Matthias Möller [b], Chungang Zhu [a,c,*]

[a] School of Mathematical Sciences, Dalian University of Technology, Dalian, 116024, China
[b] Delft Institute of Applied Mathematics, Delft University of Technology, Delft, 2628 CD, The Netherlands
[c] Key Laboratory for Computational Mathematics and Data Intelligence of Liaoning Province, Dalian, 116024, China

ARTICLE INFO

Keywords:
Isogeometric analysis
r-adaptivity
Parameterization
Weak-discontinuous problems
Enrichment methods

ABSTRACT

This paper proposes an extended *r*-adaptive isogeometric analysis framework for problems exhibiting weak discontinuities in solution derivatives, where discretization errors are often dominated by insufficient resolution of material interfaces. The method combines enrichment functions with a control-point relocation strategy guided by a Gaussian monitor constructed from an aggregated level-set representation of the interfaces. Rather than refining the mesh, resolution is redistributed according to interface geometry, enabling sharp representation of gradient jumps while preserving exact CAD geometry, spline topology, and a fixed number of degrees of freedom. Benchmark examples indicate up to 65.7% error reduction relative to enrichment-only formulations, and even larger improvements compared with standard IGA, while introducing less than 1% additional computational cost. The results demonstrate that redistributing geometric resolution provides an efficient alternative to conventional refinement-based adaptive strategies for weak-discontinuous problems.

1. Introduction

Material interfaces are ubiquitous in engineering applications involving composite media, layered structures, porous solids, and heterogeneous diffusion processes. In many such settings, the primary solution field remains continuous across the interface, whereas its gradient exhibits jumps induced by discontinuous material coefficients. Such so-called weak discontinuities arise, for example, in elasticity with inclusions, heat conduction in multi-phase materials, and transport in stratified media [1]. Although the governing equations are typically elliptic in nature, sharp interface-localized variations continue to pose significant challenges for numerical approximation and frequently result in degraded accuracy unless the discretization is carefully adapted to the interface geometry. Representative engineering and biomedical examples are shown in Fig. 1.

In classical finite element discretizations, weak discontinuities are typically handled by interface-fitted meshes or strong local refinement, both of which become cumbersome for complex geometries. Enrichment strategies based on partition-of-unity concepts [2], such as the eXtended Finite Element Method (XFEM) [3,4], alleviate this difficulty by embedding interface-aware functions into the approximation space. Isogeometric analysis (IGA) [5,6] offers an attractive alternative by employing spline and NURBS basis functions for both geometric representation and solution approximation, thereby enabling exact CAD geometry and high-order smoothness. However, precisely this smoothness renders standard IGA ill-suited for weak-discontinuous problems unless the spline mesh is aligned with the interface or aggressively refined.

To overcome this limitation, extended isogeometric formulations, commonly referred to as eXtended IsoGeometric Analysis (XIGA), introduce interface-sensitive enrichment functions through partition-of-unity techniques [9]. While XIGA can effectively capture gradient jumps, it increases the number of degrees of freedom and typically requires specialized quadrature rules on cut elements, thereby raising both implementation complexity and computational cost [10,11]. From a complementary geometric perspective, *r*-adaptive strategies relocate spline control points within a fixed topology in order to concentrate resolution near regions of pronounced solution variation [12,13]. Such mesh-movement approaches preserve the CAD representation and the continuity of the spline space; however, when used in isolation, they cannot reproduce the intrinsic derivative jumps associated with weak discontinuities [14]. Recent work [15] further demonstrated that combining local *h*-refinement with *r*-refinement in an optimal-transport framework can improve the resolution of IGA.

☆ This article is part of a Special issue entitled: 'SPM 2026' published in Computer-Aided Design.

* Corresponding authors.
E-mail addresses: y.ji-1@tudelft.nl (Y. Ji), cgzhu@dlut.edu.cn (C. Zhu).

https://doi.org/10.1016/j.cad.2026.104108
Received 29 April 2026; Accepted 21 May 2026
Available online 28 May 2026

(a) (b)

Fig. 1. Representative engineering and biomedical application examples involving pronounced material interfaces: (a) reinforced concrete beam with steel reinforcements embedded in a cementitious matrix [7]; (b) dental implant embedded in cortical and trabecular bone, characterized by strong stiffness contrast and interfacial stress concentrations [8].

These considerations motivate the present study. We propose an extended *r*-adaptive isogeometric analysis framework that integrates partition-of-unity enrichment with interface-aware control-point relocation. The enrichment functions endow the approximation space with the ability to represent gradient jumps across material interfaces, while the *r*-adaptive strategy acts as a spline reparameterization mechanism, redistributing resolution toward interface regions. Crucially, this geometric adaptation preserves the CAD model and the topology of the spline space, and does not introduce additional basis functions or alter global continuity.

The main contributions of this paper are summarized as follows:

(1) A coupled enrichment and *r*-adaptive strategy within the isogeometric analysis framework is developed for problems with weak discontinuities.
(2) A Gaussian monitor function based on an aggregated level-set description of material interfaces is constructed to redistribute geometric resolution according to interface geometry rather than mesh refinement.
(3) The proposed approach preserves exact CAD geometry and spline topology, maintaining global continuity while keeping the number of basis functions unchanged.
(4) Numerical benchmarks demonstrate that the extended *r*-adaptive IGA significantly outperforms standard IGA, extended IGA without adaptivity, and classical *h*-refined schemes in terms of both accuracy and computational efficiency.

The remainder of this paper is organized as follows. Section 2 formulates the governing weak-discontinuous problems and discusses the associated numerical challenges. Section 3 presents the extended isogeometric approximation. Section 4 introduces the proposed geometry-aware *r*-adaptive control-point relocation strategy and its coupling with enrichment. Section 5 reports the numerical experiments, and Section 6 concludes the paper.

2. Preliminaries

This section formulates the model weak-discontinuous problem and recalls the essential ingredients of isogeometric analysis needed for the proposed methodology. For simplicity and without loss of generality, we restrict the presentation to two-dimensional linear elasticity with weak discontinuities. This setting allows us to clearly introduce the notation, functional framework, and variational formulation underlying the extended *r*-adaptive isogeometric approach developed in the subsequent sections.

2.1. Fundamental equations

Let $\Omega \subset \mathbb{R}^2$ be an open bounded domain containing a set of internal material interfaces Γ_I^k, $k = 1, 2, \dots, N_{\text{faces}}$, which partition Ω into subregions with distinct material properties. The exterior boundary $\partial\Omega$ is decomposed into Dirichlet and Neumann parts,

$$\partial\Omega = \Gamma_u \cup \Gamma_t, \qquad \Gamma_u \cap \Gamma_t = \emptyset. \tag{1}$$

Let $\mathbf{u} : \Omega \to \mathbb{R}^2$ denote the displacement field and $\boldsymbol{\sigma}$ the Cauchy stress tensor. The equilibrium problem reads

$$\begin{aligned} \nabla\cdot\boldsymbol{\sigma} + \mathbf{b} &= 0 \quad \text{in } \Omega, \\ \mathbf{u} &= \bar{\mathbf{u}} \quad \text{on } \Gamma_u, \\ \boldsymbol{\sigma}\mathbf{n} &= \bar{\mathbf{t}} \quad \text{on } \Gamma_t. \end{aligned} \tag{2}$$

Across each interface Γ_I^k the displacement field is continuous while the stresses satisfy traction continuity,

$$[\![\mathbf{u}]\!] = 0, \ [\![\boldsymbol{\sigma}\mathbf{n}_I^k]\!] = 0, \ \text{on } \Gamma_I^k, \ k = 1, \dots, N_{\text{faces}}. \tag{3}$$

These conditions characterize a weak discontinuity, since material parameters are discontinuous across Γ_I^k and therefore the displacement gradient may exhibit jumps.

Here $\mathbf{b}$ denotes the body-force density, $\mathbf{n}$ the outward unit normal on $\partial\Omega$, and $\mathbf{n}_I^k$ a chosen unit normal defining the orientation of Γ_I^k. For any quantity $\mathbf{v}$ possessing traces on Γ_I^k, the jump operator is defined as

$$[\![\mathbf{v}]\!] := \mathbf{v}^+ - \mathbf{v}^-, \tag{4}$$

where $(\cdot)^\pm$ denote traces taken from the two sides of Γ_I^k, with the '+' side corresponding to the direction of $\mathbf{n}_I^k$.

We consider infinitesimal strains and small deformations. The strain tensor is defined by the symmetric gradient

$$\boldsymbol{\varepsilon}(\mathbf{u}) = \nabla_s\mathbf{u} := \tfrac{1}{2}\left(\nabla\mathbf{u} + (\nabla\mathbf{u})^\top\right), \tag{5}$$

and the constitutive law is given by Hooke's relation

$$\boldsymbol{\sigma} = \mathbb{D} : \boldsymbol{\varepsilon}. \tag{6}$$

The fourth-order elasticity tensor $\mathbb{D}$ is symmetric positive definite and piecewise constant on each material subdomain.

For the discretization it is convenient to employ Voigt notation,

$$\boldsymbol{\varepsilon} = [\varepsilon_{xx}, \varepsilon_{yy}, \varepsilon_{xy}]^\top, \qquad \boldsymbol{\sigma} = [\sigma_{xx}, \sigma_{yy}, \sigma_{xy}]^\top, \tag{7}$$

so that the constitutive relation reduces to the matrix form

$$\boldsymbol{\sigma} = \mathbb{D}\,\boldsymbol{\varepsilon}, \qquad \boldsymbol{\varepsilon} = \mathbb{C}\,\boldsymbol{\sigma}, \tag{8}$$

where $\mathbb{C} = \mathbb{D}^{-1}$ denotes the compliance matrix.

By standard variational arguments, the equilibrium displacement field is characterized as the minimizer of the total potential energy functional

$$\Pi(\mathbf{u}) := U(\mathbf{u}) - W(\mathbf{u}) \tag{9}$$

over the admissible space $\mathcal{U}$.

The strain energy is given by

$$U(\mathbf{u}) = \frac{1}{2}\int_\Omega \boldsymbol{\varepsilon}(\mathbf{u}) : \mathbb{D} : \boldsymbol{\varepsilon}(\mathbf{u})\,\mathrm{d}\Omega, \tag{10}$$

while the external work reads

$$W(\mathbf{u}) = \int_\Omega \mathbf{u}\cdot\mathbf{b}\,\mathrm{d}\Omega + \int_{\Gamma_t} \mathbf{u}\cdot\bar{\mathbf{t}}\,\mathrm{d}\Gamma. \tag{11}$$

Let the trial and test spaces be defined as

$$\mathcal{U} = \{\mathbf{u} \in H^1(\Omega) \mid \mathbf{u} = \bar{\mathbf{u}} \text{ on } \Gamma_u\}, \tag{12}$$

and

$$\mathcal{V} = \{\mathbf{v} \in H^1(\Omega) \mid \mathbf{v} = 0 \text{ on } \Gamma_u\}. \tag{13}$$

The weak formulation of the elasticity interface problem reads: find $\mathbf{u} \in \mathcal{U}$ such that

$$a(\mathbf{u}, \mathbf{v}) = \ell(\mathbf{v}) \qquad \forall \mathbf{v} \in \mathcal{V}, \tag{14}$$

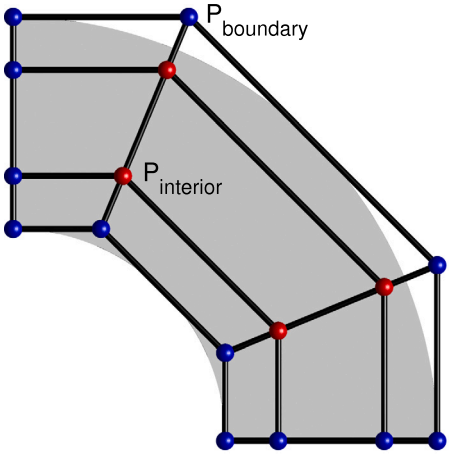

Fig. 2. Schematic illustration of interior and boundary control points in an isogeometric parameterization. Boundary control points remain fixed, whereas interior control points act as geometric degrees of freedom. Relocating interior control points modifies the geometric parameterization while preserving the spline topology and bijectivity, which forms the basis of the proposed *r*-adaptive strategy.

with bilinear and linear forms

$$a(\mathbf{u},\mathbf{v}) = \int_{\Omega} \boldsymbol{\varepsilon}(\mathbf{u}) : \mathbb{D} : \boldsymbol{\varepsilon}(\mathbf{v})\, \mathrm{d}\Omega, \tag{15}$$

$$\ell(\mathbf{v}) = \int_{\Omega} \mathbf{v}\cdot\mathbf{b}\, \mathrm{d}\Omega + \int_{\Gamma_t} \mathbf{v}\cdot\bar{\mathbf{t}}\, \mathrm{d}\Gamma. \tag{16}$$

2.2. Geometric parameterization and isogeometric discretization

In isogeometric analysis, spline functions are used both to parameterize the computational domain and to approximate the solution fields. Let $\hat{\Omega}$ denote the parametric domain, equipped with tensor-product knot vectors

$$\Xi = \{\xi_0, \xi_1, \ldots, \xi_{n+p+1}\}, \tag{17}$$

and

$$\mathcal{H} = \{\eta_0, \eta_1, \ldots, \eta_{m+q+1}\}, \tag{18}$$

with polynomial degrees p and q in the two parametric directions.

Let $\hat{\Omega}$ denote the parametric domain. The physical domain Ω is represented by the image of $\hat{\Omega}$ under the geometric parameterization

$$\boldsymbol{x}(\xi,\eta) = \sum_{i=1}^{n}\sum_{j=1}^{m} N_{i,p}(\xi)\, M_{j,q}(\eta)\, \mathbf{P}_{ij}, \tag{19}$$

where $\mathbf{P}_{ij} \in \mathbb{R}^2$ are the control points and $N_{i,p}(\xi)$ and $M_{j,q}(\eta)$ denote the B-spline basis functions defined recursively via the Cox–de Boor formula [16].

Fig. 2 illustrates a tensor-product B-spline parameterization of a quarter annulus. Under standard assumptions, the mapping $\boldsymbol{x} : \hat{\Omega} \to \Omega$ is assumed to be bijective with $\det(\nabla_{\xi}\boldsymbol{x}) > 0$ everywhere in $\hat{\Omega}$.

In isogeometric analysis, the integration of the weak form in Eq. (14) is carried out by evaluating the basis functions in the parametric domain and transforming the integrals to the physical domain through Eq. (19), followed by the assembly and solution of the resulting linear system. A fundamental aspect of isogeometric analysis is that the control point positions directly govern both the geometric parameterization quality and the accuracy of the numerical solution.

In the following, the set of control points is partitioned into interior and boundary subsets, $\mathcal{I}_I$ and $\mathcal{I}_B$, respectively. Boundary control points $\mathbf{P}_{i_2}$ with $i_2 \in \mathcal{I}_B$ are assumed to be fixed, whereas the interior control points $\mathbf{P}_{i_1}$ with $i_1 \in \mathcal{I}_I$ are regarded as design variables. The geometric parameterization can therefore be written as

$$\boldsymbol{x}(\xi,\eta) = \sum_{i_1\in\mathcal{I}_I} N_{i_1}(\xi,\eta)\, \mathbf{P}_{i_1} + \sum_{i_2\in\mathcal{I}_B} N_{i_2}(\xi,\eta)\, \mathbf{P}_{i_2}, \tag{20}$$

where $N_{i_1}(\xi,\eta)$ and $N_{i_2}(\xi,\eta)$ denote the tensor-product B-spline basis functions associated with the interior and boundary control points, respectively.

As shown in Fig. 2, relocating the interior control points enables one to modify the geometric parameterization while preserving the spline topology and the bijectivity of the geometry [17]. Such geometric degrees of freedom may be exploited either to improve mapping quality indicators, such as orthogonality and smoothness, leading to isotropic parameterizations, or to introduce anisotropic distributions tailored to solution features [13]. This observation forms the basis of the *r*-adaptive parameterization strategy developed in the next section, in which the interior control points are iteratively relocated according to a weak-discontinuous-oriented monitor function.

3. Extended isogeometric formulation for weak-discontinuous problems

This section presents the extended isogeometric formulation for problems with weak discontinuities. The formulation comprises three main components: a level-set-based enrichment strategy within the IGA framework, a quadrature treatment for interface-cut elements, and a strain-recovery procedure used to construct the error measures.

3.1. Extended isogeometric approximation

To accurately capture weak discontinuities without excessive mesh refinement, the extended isogeometric analysis augments the standard IGA approximation by incorporating problem-dependent enrichment functions.

The standard IGA approximation reads

$$\mathbf{u}_h(\xi) = \sum_{i\in\mathcal{N}_{\mathrm{std}}} R_i(\xi)\, \mathbf{u}_i, \tag{21}$$

where $\boldsymbol{\xi} = (\xi,\eta)^{\top} \in \hat{\Omega}$ denotes the parametric coordinates, $R_i(\xi)$ denote the B-spline basis functions, and $\mathbf{u}_i$ are the associated control variables.

Following the partition-of-unity enrichment paradigm, the approximation is extended to

$$\mathbf{u}_h(\xi) = \sum_{i\in\mathcal{N}_{\mathrm{std}}} R_i(\xi)\, \mathbf{u}_i + \sum_{j\in\mathcal{N}_{\mathrm{faces}}} R_j(\xi)\, \Psi(\xi)\, \mathbf{u}_j, \tag{22}$$

where $\mathcal{N}_{\mathrm{faces}}$ denotes the set of control points whose support intersects the material interface, $\mathcal{N}_{\mathrm{std}}$ denotes the set of control points whose support does not intersect the material interface, $\mathbf{u}_j$ are the additional enrichment degrees of freedom, and $\Psi(\xi)$ is an enrichment function constructed to reproduce the jump in solution gradients across the interface.

For weak-discontinuous problems, the enrichment function is chosen as [18]

$$\Psi(\xi) = \sum_{I} |\varphi_I|\, R_I(\xi) - \left|\sum_{I} \varphi_I\, R_I(\xi)\right|, \tag{23}$$

where φ_I denotes nodal values of a level-set function $\varphi(\boldsymbol{x})$ describing the interface. The shift–subtraction structure ensures that the enrichment preserves the partition-of-unity property. The resulting approximation is C^0 but not C^1 across the interface, which is consistent with the regularity of weak discontinuities.

The material interface Γ_I^k is implicitly represented by the zero-level set of $\varphi^{(k)}(\boldsymbol{x})$ [19,20],

$$\Gamma_I^k = \{\boldsymbol{x} \in \mathbb{R}^2 : \varphi^{(k)}(\boldsymbol{x}) = 0\}, \tag{24}$$

where $\varphi^{(k)}(\boldsymbol{x}) > 0$ and $\varphi^{(k)}(\boldsymbol{x}) < 0$ correspond to the two material subdomains. In practice, $\varphi^{(k)}(\boldsymbol{x})$ is often taken as a signed-distance function,

$$\varphi^{(k)}(\boldsymbol{x}) = \pm \min_{\mathbf{y}\in\Gamma_I^k} \|\boldsymbol{x}-\mathbf{y}\|. \tag{25}$$

Control points whose support intersects the zero-level set are classified as enriched and collected in the set $\mathcal{N}_{\text{faces}}$.

Insertion of the enriched approximation (22) into the weak formulation (14) and testing with the corresponding basis functions leads to the linear system

$$\mathbf{K}\mathbf{U} = \mathbf{F}. \tag{26}$$

The global vector of unknowns is partitioned into standard and enriched degrees of freedom,

$$\mathbf{U} = \begin{bmatrix} \mathbf{U}^{\text{std}} \\ \mathbf{U}^{\text{enr}} \end{bmatrix}. \tag{27}$$

Accordingly, the stiffness matrix admits the block structure

$$\mathbf{K} = \begin{bmatrix} \mathbf{K}^{\text{std,std}} & \mathbf{K}^{\text{std,enr}} \\ \mathbf{K}^{\text{enr,std}} & \mathbf{K}^{\text{enr,enr}} \end{bmatrix}. \tag{28}$$

At the element level, the stiffness matrix is assembled from the bilinear form. For instance, the standard–enriched coupling block reads

$$\mathbf{K}_e^{\text{std,enr}} = \int_{\Omega_e} (\mathbf{B}_e^{\text{std}})^{\mathsf{T}} \mathbb{D} \mathbf{B}_e^{\text{enr}} \, \mathrm{d}\Omega_e, \tag{29}$$

while the remaining blocks are obtained analogously.

The strain–displacement matrices associated with the standard and enriched basis functions are

$$\mathbf{B}_i^{\text{std}} = \begin{bmatrix} \partial_x R_i & 0 \\ 0 & \partial_y R_i \\ \partial_y R_i & \partial_x R_i \end{bmatrix}, \qquad \mathbf{B}_i^{\text{enr}} = \begin{bmatrix} \partial_x (R_i \Psi) & 0 \\ 0 & \partial_y (R_i \Psi) \\ \partial_y (R_i \Psi) & \partial_x (R_i \Psi) \end{bmatrix}.$$

The corresponding load vector follows from the linear functional $\ell(\cdot)$ in Eq. (16), i.e.,

$$\mathbf{F}_i^{\text{std}} = \int_\Omega \mathbf{b}\, R_i \, \mathrm{d}\Omega, \qquad \mathbf{F}_i^{\text{enr}} = \int_\Omega \mathbf{b}\, R_i \Psi \, \mathrm{d}\Omega. \tag{30}$$

3.2. Numerical integration for cut elements

In extended isogeometric discretizations, elements intersected by material interfaces Γ_I^k give rise to integrands that are only piecewise smooth due to the presence of gradient discontinuities induced by the enrichment functions. As a consequence, conventional tensor-product Gauss quadrature may yield suboptimal accuracy when applied directly to such interface-cut elements.

To accurately evaluate the element matrices, we adopt a triangular subcell integration strategy. Each cut element is subdivided into a set of subtriangles that conform to the interface geometry, ensuring that the integrands remain smooth within each subcell. Numerical integration is then performed on every subtriangle using a 13-point Gaussian rule [9,21]. For elements not intersected by the interface, the standard tensor-product Gauss rule with $(p+1)\times(q+1)$ quadrature points is adopted.

Fig. 3 illustrates the resulting quadrature distribution for both standard and interface-cut elements. While conventional elements employ tensor-product Gauss points, interface-cut elements are subdivided into triangular subcells aligned with the interface geometry, thereby ensuring accurate evaluation of the enriched contributions without altering the spline discretization.

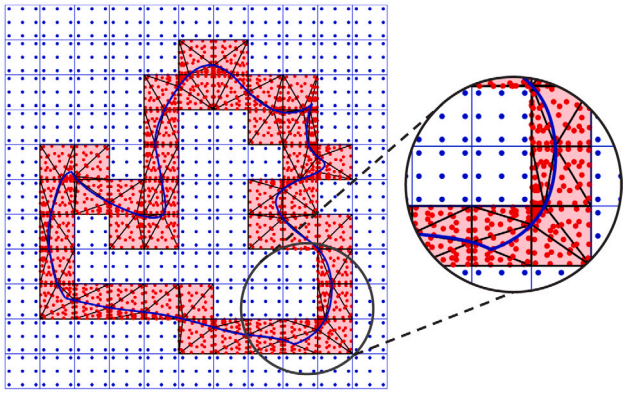

Fig. 3. Sub-triangulation of elements intersected by the inclusion geometry together with the corresponding Gauss quadrature points adopted for numerical integration in the XIGA method.

3.3. Strain recovery and error indicators

Following the superconvergent patch recovery (SPR) technique of Zienkiewicz and Zhu [22], we construct a smoothed strain field $\boldsymbol{\varepsilon}^s$ by projecting the computed strain $\boldsymbol{\varepsilon}^h$ onto the same spline space employed for the displacement approximation $\mathbf{u}_h$.

In the presence of material interfaces, the recovered field is enriched by interface-dependent enrichment contributions, leading to

$$\boldsymbol{\varepsilon}^s(\boldsymbol{x}) = \sum_{i\in\mathcal{N}_{\text{std}}} R_i(\boldsymbol{x})\, \mathbf{e}_i + \sum_{k=1}^{N_{\text{faces}}} \sum_{j\in\mathcal{N}_{\text{faces}}^k} R_j(\boldsymbol{x}) \left(H_k(\boldsymbol{x}) - H_k(\mathbf{P}_j)\right) \mathbf{e}_j^k, \tag{31}$$

where $\mathbf{e}_i \in \mathbb{R}^3$ and $\mathbf{e}_j^k \in \mathbb{R}^3$ denote the unknown recovery coefficients associated with the standard and interface-enriched spline basis functions, respectively, determined from a least-squares projection of the computed strain field. Here $\mathbf{P}_j$ is the physical coordinate of the jth control point.

The function $H_k(\boldsymbol{x})$ denotes the generalized Heaviside function associated with the kth interface, defined in terms of the corresponding level-set function $\varphi^{(k)}(\boldsymbol{x})$ as

$$H_k(\boldsymbol{x}) = \begin{cases} +1, & \varphi^{(k)}(\boldsymbol{x}) \geq 0, \\ -1, & \varphi^{(k)}(\boldsymbol{x}) < 0. \end{cases} \tag{32}$$

The shifted enrichment $H_k(\boldsymbol{x}) - H_k(\mathbf{P}_j)$ ensures consistency with the partition-of-unity structure of the spline basis.

To obtain a smooth strain representation compatible with material interfaces, we construct an enriched recovery space and approximate the recovered strain field as

$$\boldsymbol{\varepsilon}^s(\boldsymbol{x}) = \mathbf{R}^*(\boldsymbol{x})\, \boldsymbol{\alpha}^*, \tag{33}$$

where $\boldsymbol{\varepsilon}^s \in \mathbb{R}^3$ denotes the strain vector in Voigt notation and $\boldsymbol{\alpha}^* \in \mathbb{R}^{n^*}$ collects the recovery coefficients associated with standard and interface-enriched basis functions.

The recovery matrix is decomposed into standard and enriched contributions,

$$\mathbf{R}^*(\boldsymbol{x}) = \left[\mathbf{R}_{\text{std}}^*(\boldsymbol{x}) \;\; \mathbf{R}_{\text{enr}}^*(\boldsymbol{x})\right]. \tag{34}$$

In two dimensions,

$$\mathbf{R}_{\text{std}}^* = \mathbf{I}_3 \otimes \mathbf{R}_{\text{std}}, \qquad \mathbf{R}_{\text{enr}}^* = \mathbf{I}_3 \otimes \mathbf{R}_{\text{enr}}, \tag{35}$$

where, for a given interface Γ_I^k,

$$\mathbf{R}_{\text{enr}} = \left[R_j(\boldsymbol{x})\big(H_k(\boldsymbol{x}) - H_k(\mathbf{P}_j)\big)\right]_{j\in\mathcal{I}_k}, \tag{36}$$

and $\mathcal{I}_k$ denotes the set of control points enriched by Γ_I^k.

The coefficients $\boldsymbol{\alpha}^*$ are obtained by the L^2-projection of the discrete strain field $\boldsymbol{\varepsilon}^h$ onto the recovery space, i.e.,

$$J(\boldsymbol{\alpha}^*) = \frac{1}{2}\int_{\Omega} \|\mathbf{R}^*(\boldsymbol{x})\boldsymbol{\alpha}^* - \boldsymbol{\varepsilon}^h(\boldsymbol{x})\|^2 \,\mathrm{d}\Omega. \tag{37}$$

The minimizer satisfies the normal equations

$$\mathbf{A}\,\boldsymbol{\alpha}^* = \mathbf{b}^*, \tag{38}$$

where

$$\mathbf{A} = \int_{\Omega} (\mathbf{R}^*)^{\top}\mathbf{R}^* \,\mathrm{d}\Omega, \tag{39}$$

and

$$\mathbf{b}^* = \int_{\Omega} (\mathbf{R}^*)^{\top}\boldsymbol{\varepsilon}^h \,\mathrm{d}\Omega. \tag{40}$$

Provided the recovery basis functions are linearly independent in Ω, the matrix $\mathbf{A}$ is symmetric positive definite and the least-squares solution is unique.

The recovered strain is subsequently used to define energy-norm error indicators in Section 5 driving the proposed r-adaptive relocation of control points.

For a strain field $\boldsymbol{\varepsilon}$, we define the energy norm [23]

$$\|\boldsymbol{\varepsilon}\|_{E(\Omega)} = \left(\frac{1}{2}\int_{\Omega} \boldsymbol{\varepsilon}^{\top}\mathbb{D}\boldsymbol{\varepsilon} \,\mathrm{d}\Omega\right)^{1/2}. \tag{41}$$

If the exact strain field $\boldsymbol{\varepsilon}$ is available, the exact error in energy norm reads

$$\|e\|_{E(\Omega)} = \|\boldsymbol{\varepsilon} - \boldsymbol{\varepsilon}^h\|_{E(\Omega)}, \tag{42}$$

with corresponding relative error

$$\|e_r\|_{E(\Omega)} = \frac{\|e\|_{E(\Omega)}}{\|\boldsymbol{\varepsilon}\|_{E(\Omega)}} \times 100\%. \tag{43}$$

In practical computations, where the exact solution is unavailable, we replace $\boldsymbol{\varepsilon}$ by the recovered strain field $\boldsymbol{\varepsilon}^s$ and define the recovery-based error estimator

$$\|e^s\|_{E(\Omega)} = \|\boldsymbol{\varepsilon}^s - \boldsymbol{\varepsilon}^h\|_{E(\Omega)}, \tag{44}$$

together with the relative estimator

$$\|e^s_r\|_{E(\Omega)} = \frac{\|e^s\|_{E(\Omega)}}{\|\boldsymbol{\varepsilon}^s\|_{E(\Omega)}} \times 100\%. \tag{45}$$

4. Interface-aware r-adaptive isogeometric analysis for weak-discontinuous problems

Although enrichment techniques such as XIGA accurately represent weak discontinuities across material interfaces, they do not regulate the geometric distribution of resolution. With a uniform parameterization, sharp gradients caused by material contrast are often misaligned with the spline mapping, resulting in locally inadequate approximation quality even in enriched formulations.

To address this limitation, an interface-aware r-adaptive strategy is introduced within the extended isogeometric framework. The method relocates interior control points in the parametric domain while preserving the spline topology, knot vectors, and total number of degrees of freedom. By concentrating geometric resolution near material interfaces and regions of high error, the approach complements the enriched approximation and improves accuracy without increasing the number of unknowns. Fig. 4 illustrates the main components of the framework, including interface aggregation, monitor construction, parametric redistribution, and enriched analysis.

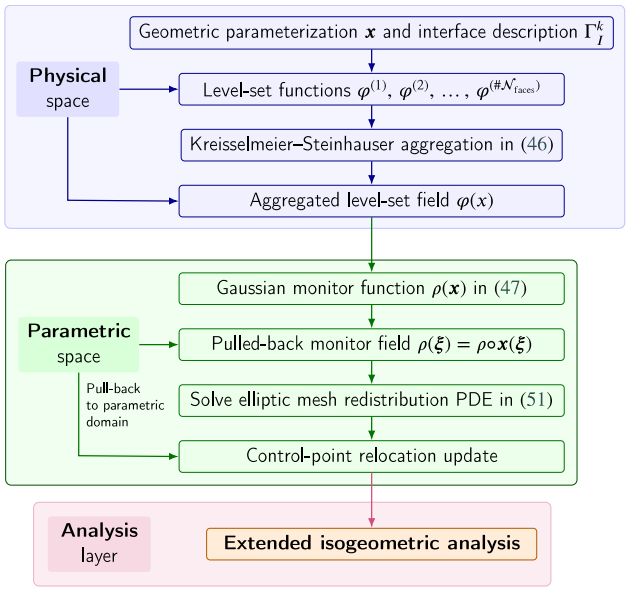

Fig. 4. Overview of the proposed interface-aware r-adaptive XIGA framework. Multiple level-set functions describing material interfaces are aggregated using a KS operator to form a smooth interface indicator. A Gaussian monitor function is constructed in the physical domain and pulled back to the parametric domain, where a weighted elliptic redistribution relocates interior control points while preserving the spline space. The resulting parameterization is then employed in the enriched XIGA analysis.

4.1. Interface-aware monitor function for r-adaptivity

The r-adaptive redistribution is driven by a scalar monitor function ρ that prescribes the desired spatial concentration of geometric resolution in the physical domain. For weak-discontinuous problems, sharp gradients typically arise near material interfaces due to jumps in material properties. Accordingly, the monitor function is constructed from an implicit interface representation based on level-set functions.

Let $\varphi^{(k)}(\boldsymbol{x})$, $k = 1, 2, \ldots, N_{\text{faces}}$, denote individual level-set functions whose zero level sets describe the material interfaces. Figs. 5(a)–5(c) show representative level-set contours corresponding to three distinct inclusions forming a multi-interface configuration.

To obtain a single smooth scalar field measuring the distance to the nearest interface, we employ a smooth minimum based on Kreisselmeier–Steinhauser (KS) aggregation and define

$$\varphi(\boldsymbol{x}) = -\frac{1}{\beta}\ln\left(\sum_{k=1}^{N_{\text{faces}}} \exp\left(-\beta\,\varphi^{(k)}(\boldsymbol{x})\right)\right), \tag{46}$$

where $\beta > 0$ controls the sharpness of the approximation. As $\beta \to \infty$, $\varphi(\boldsymbol{x})$ converges to the pointwise minimum $\min_k \varphi^{(k)}(\boldsymbol{x})$.

The KS operator provides a continuously differentiable approximation of the minimum operator, ensuring that $\nabla\varphi$ exists everywhere. This smoothness is essential for constructing a well-behaved monitor function and for maintaining stability of the subsequent elliptic redistribution equation. The aggregated level-set field is shown in Fig. 5(d), whose zero contour represents the union of all interfaces in a unified smooth form.

Based on the aggregated level-set field, the monitor function is defined as

$$\rho(\boldsymbol{x}) = \rho_0 + \alpha\exp\left(-\left(\frac{|\varphi(\boldsymbol{x})|}{\delta}\right)^2\right), \tag{47}$$

where $\rho_0 > 0$ denotes the background density, $\alpha > 0$ controls the strength of interface-driven concentration, and $\delta > 0$ determines the width of the refinement band.

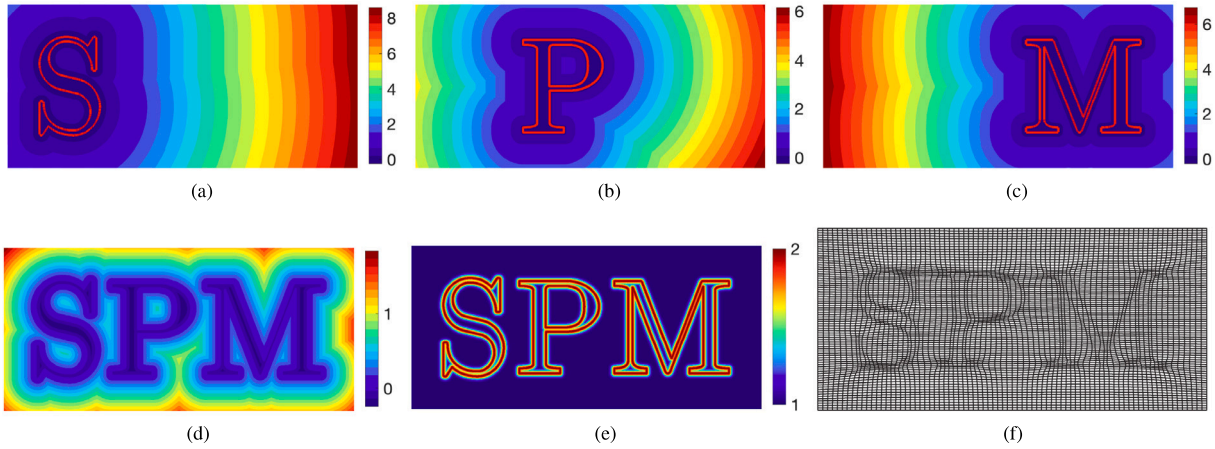

Fig. 5. Interface-aware monitor construction and *r*-adaptive parameterization for a multi-inclusion configuration: (a)–(c) individual level-set fields for the three interfaces forming the letters "S", "P", and "M"; (d) KS-aggregated level-set field $\varphi(\boldsymbol{x})$; (e) Gaussian-type monitor $\rho(\boldsymbol{x})$ generated from $\varphi(\boldsymbol{x})$, highlighting refinement zones around all interfaces; (f) resulting *two-dimensional* r-adapted parameterization on the same planar domain as panels (a)–(e), visualized through its iso-parametric lines; the dark regions near the letter interfaces correspond to strongly compressed iso-parametric lines in the high-density zones of $\rho(\boldsymbol{x})$.

The monitor attains its maximum value $\rho_{\max} = \rho_0 + \alpha$ at the interface ($\varphi = 0$) and decays smoothly to the background level ρ_0 away from the interface. The Gaussian profile yields a smooth metric field, thereby preventing abrupt spatial variations that may degrade the quality of the redistributed parameterization. Fig. 5(e) shows the resulting monitor field for the multi-interface configuration, where refinement zones are automatically generated around all interfaces.

In the implementation, the monitor function ρ is evaluated on the initial geometry at quadrature points and pulled back to the parametric domain $\hat{\Omega}$ through the geometric parameterization $\boldsymbol{x}$, i.e.,

$$\rho(\boldsymbol{\xi}) = \rho \circ \boldsymbol{x}(\boldsymbol{\xi}). \tag{48}$$

The resulting parametric monitor field is kept fixed and defines the metric in the elliptic redistribution equation. Interior control points are relocated accordingly while preserving the topology and the total number of DOFs. Note that the interfaces themselves are not conformed to by the resulting parameterization; they remain represented implicitly through the level-set field $\varphi(\boldsymbol{x})$, and the role of the *r*-adaptive redistribution is solely to concentrate the parametric resolution in their vicinity.

4.2. Unified treatment of multiple interfaces

In many engineering applications, material interfaces appear in clusters rather than in isolation, as in fiber-reinforced composites, porous media, or components containing multiple inclusions. In such situations, several interfaces may simultaneously induce pronounced local gradients, requiring a coordinated resolution strategy [24].

Within the present framework, each interface Γ_I^k, $k = 1, 2, \ldots, N_{\text{faces}}$, is represented implicitly by a level-set function $\varphi^{(k)}(\boldsymbol{x})$ whose zero level set defines the interface location. Rather than treating interfaces individually during adaptation, a single smooth scalar field is constructed by aggregating the level-set functions using the KS operator introduced in (46). The resulting field

$$\varphi(\boldsymbol{x}) \approx \min_{k \in \mathcal{N}_{\text{faces}}} \varphi^{(k)}(\boldsymbol{x}), \tag{49}$$

provides a differentiable approximation of the distance to the nearest interface and allows all interfaces to be handled simultaneously within a unified *r*-adaptive update.

This aggregation strategy provides several important properties. First, it eliminates the need for interface-specific adaptive loops and prevents conflicting control-point motions when inclusions are located in close proximity. Second, the smooth KS approximation preserves differentiability of the monitor function, which is required for the well-posedness of the elliptic redistribution equations governing the control-point relocation. Third, the formulation extends naturally to an arbitrary number of interfaces without any modification of the underlying isogeometric discretization.

When coupled with the Gaussian-type monitor (47), the aggregated level-set field automatically generates refinement zones around all interfaces, including strongly interacting clusters, while leaving regions far from interfaces essentially unchanged. This behavior is particularly relevant for the numerical experiments in Section 5, where multiple inclusions give rise to overlapping high-gradient regions.

In practice, the level-set functions are evaluated in the physical domain Ω, aggregated using (46), and sampled at quadrature points before being pulled back to the parametric domain $\hat{\Omega}$. The resulting monitor field $\rho(\boldsymbol{\xi})$ is kept fixed within each redistribution cycle and is used to assemble the elliptic operator that updates the interior control-point positions.

4.3. PDE-based r-adaptive parameterization

The proposed adaptive strategy is realized through the relocation of interior control points only, while leaving the knot vectors, polynomial degrees, weights, and spline topology unchanged. Hence, the geometric parameterization remains fully CAD-compatible, and the total number of degrees of freedom is preserved during the entire procedure.

Let $\boldsymbol{\xi} = (\xi, \eta) \in \hat{\Omega}$ denote the parametric domain and let $\boldsymbol{x}(\boldsymbol{\xi})$ represent the associated geometric parameterization defined by the NURBS surface. The mesh redistribution problem is formulated directly in $\hat{\Omega}$, where the physical coordinates of the control mesh are treated as unknown fields

$$\boldsymbol{x}(\boldsymbol{\xi}) = (x(\boldsymbol{\xi}), y(\boldsymbol{\xi}))^{\top}. \tag{50}$$

Given the monitor function $\rho(\boldsymbol{x})$ introduced in Eq. (47), its pull-back to the parametric domain is defined by Eq. (48) and is evaluated on the current geometry and kept fixed within each redistribution cycle.

The updated control-point positions are obtained by solving the weighted elliptic system

$$\nabla_{\boldsymbol{\xi}} \cdot \left(\rho(\boldsymbol{\xi}) \nabla_{\boldsymbol{\xi}} \boldsymbol{x} \right) = \boldsymbol{0} \qquad \text{in } \hat{\Omega}, \tag{51}$$

subject to Dirichlet boundary conditions fixing the boundary control points.

Eq. (51) can be interpreted as the Euler–Lagrange equations of the geometric functional

$$\mathcal{J}_{\text{geo}}(\boldsymbol{x}) = \frac{1}{2} \int_{\hat{\Omega}} \rho(\boldsymbol{\xi}) \left\| \nabla_{\boldsymbol{\xi}} \boldsymbol{x} \right\|^2 \, \mathrm{d}\boldsymbol{\xi}, \tag{52}$$

which promotes an approximately uniform distribution of the weighted metric tensor $\rho\,\nabla_{\xi}\boldsymbol{x}$. Regions where ρ is large therefore induce locally compressed parameter lines, leading to a concentration of control points in the corresponding physical regions.

The weak form of (51) is discretized using the same spline space that defines the geometric parameterization. After splitting the control point indices into an interior set $\mathcal{I}_{\mathrm{f}}$ (free degrees of freedom) and a boundary set $\mathcal{I}_{\mathrm{b}}$ (prescribed on Γ_u), the discretization yields the symmetric positive-definite linear system

$$\mathbf{K}_{\mathrm{ff}}\,\mathbf{X}_{\mathrm{f}} = -\,\mathbf{K}_{\mathrm{fb}}\,\mathbf{X}_{\mathrm{b}}, \tag{53}$$

where $\mathbf{X}_{\mathrm{f}}$ and $\mathbf{X}_{\mathrm{b}}$ collect the coordinates of the interior and boundary control points, respectively, and the block matrices are defined component-wise by

$$(\mathbf{K}_{\mathrm{ff}})_{ij} = \int_{\hat{\Omega}} \rho(\boldsymbol{\xi})\,\nabla_{\xi} N_i(\boldsymbol{\xi}) \cdot \nabla_{\xi} N_j(\boldsymbol{\xi})\,\mathrm{d}\boldsymbol{\xi},\ \ i,j \in \mathcal{I}_{\mathrm{f}}, \tag{54}$$

$$(\mathbf{K}_{\mathrm{fb}})_{ij} = \int_{\hat{\Omega}} \rho(\boldsymbol{\xi})\,\nabla_{\xi} N_i(\boldsymbol{\xi}) \cdot \nabla_{\xi} N_j(\boldsymbol{\xi})\,\mathrm{d}\boldsymbol{\xi},\ \ i \in \mathcal{I}_{\mathrm{f}},\ \ j \in \mathcal{I}_{\mathrm{b}}. \tag{55}$$

Here $\{N_i\}$ denotes the B-spline basis functions spanning the parameterization space, and the splitting $\mathcal{I}_{\mathrm{f}} \cup \mathcal{I}_{\mathrm{b}}$ distinguishes interior control points, whose positions are updated by the redistribution, from boundary control points, which are fixed in order to preserve the original CAD geometry on Γ_u.

The system (53) is solved independently for each spatial component.

The resulting r-adapted parameterization is illustrated in Fig. 5(f), where the iso-parameter lines become concentrated in regions of high monitor density. In contrast to r-adaptive parameterization approaches formulated as nonlinear optimization problems [13,25], the present method reduces each redistribution step to the solution of a symmetric positive-definite linear elliptic system. The absence of nonlinear iterations removes the dependence on initial guesses and avoids issues related to convergence to local minima.

Moreover, since no knot insertion or degree elevation is performed, the size of the redistribution system coincides with that of the geometric control mesh and remains constant throughout the adaptive process. Consequently, the computational cost of the r-adaptive update scales linearly with the number of control points and is modest compared with the extended IGA solve, as confirmed in the numerical experiments of Section 5.

5. Numerical experiments

This section presents numerical examples to evaluate the performance of the proposed r-adaptive extended isogeometric method. The tests cover configurations with increasing geometric and interface complexity, ranging from a benchmark inclusion problem with analytical solution to multi-inclusion bi-material cases. Accuracy is assessed in terms of the relative energy error and the convergence behavior under a fixed number of degrees of freedom.

All simulations were performed in double precision using MATLAB on a standard desktop computer with an Intel Core i5-13500 CPU (2.50 GHz) and 16 GB RAM.

5.1. Bi-material inclusion benchmark

The first numerical experiment considers a classical bi-material inclusion problem for which an analytical solution is available. This example is used as a quantitative benchmark to assess the accuracy and convergence behavior of the proposed r-adaptive extended IGA formulation in the presence of weak material discontinuities.

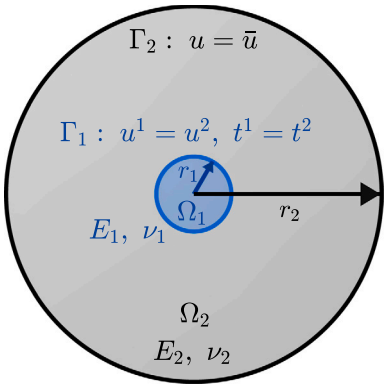

Fig. 6. Circular bi-material inclusion benchmark. A concentric inclusion Ω_1 of radius $r_1 = 0.4$ is embedded in a matrix domain Ω_2 of radius $r_2 = 2.0$. Displacement and traction continuity are enforced across the interface Γ_1, and prescribed displacement is applied on the outer boundary Γ_2.

5.1.1. Accuracy and computational cost

We consider a circular domain Ω_2 containing a concentric circular inclusion Ω_1, separated by the interface Γ_1, as illustrated in Fig. 6. The radius of the inclusion and the outer boundary are denoted by r_1 and r_2, respectively. Plane strain conditions are assumed throughout. The inclusion and matrix are characterized by elastic parameters $(E_1, \nu_1) = (1, 0.25)$ and $(E_2, \nu_2) = (10, 0.3)$, respectively. The geometric parameters are set to $r_1 = 0.4$ and $r_2 = 2.0$.

A radial displacement boundary condition is prescribed on the outer boundary Γ_2 at $r = r_2$, i.e., $u_r = r$ and $u_\theta = 0$. The problem admits an axisymmetric analytical reference solution obtained from displacement and traction continuity across the material interface [26]. The exact displacement field in polar coordinates reads

$$u_r(r) = \begin{cases} \left[(1 - \dfrac{r_2^2}{r_1^2})\alpha + \dfrac{r_2^2}{r_1^2}\right] r, & 0 \le r \le r_1, \\ \left(r - \dfrac{r_2^2}{r}\right)\alpha + \dfrac{r_2^2}{r}, & r_1 \le r \le r_2, \end{cases} \tag{56}$$

with $u_\theta = 0$, and

$$\alpha_0 = \frac{(\lambda_1 + \mu_1 + \mu_2) r_2^2}{(\lambda_2 + \mu_2) r_1^2 + (\lambda_1 + \mu_1)(r_2^2 - r_1^2) + \mu_2 r_2^2}, \tag{57}$$

where (λ_i, μ_i) denote the Lamé constants of material Ω_i, with $i = 1$ for the inclusion and $i = 2$ for the matrix.

The radial (ε_{rr}) and hoop ($\varepsilon_{\theta\theta}$) strains follow as

$$\varepsilon_{rr}(r) = \begin{cases} \left(1 - \dfrac{r_2^2}{r_1^2}\right)\alpha_0 + \dfrac{r_2^2}{r_1^2}, & 0 \le r \le r_1, \\ \left(1 + \dfrac{r_2^2}{r^2}\right)\alpha_0 - \dfrac{r_2^2}{r^2}, & r_1 \le r \le r_2, \end{cases} \tag{58}$$

$$\varepsilon_{\theta\theta}(r) = \begin{cases} \left(1 - \dfrac{r_2^2}{r_1^2}\right)\alpha_0 + \dfrac{r_2^2}{r_1^2}, & 0 \le r \le r_1, \\ \left(1 - \dfrac{r_2^2}{r^2}\right)\alpha_0 + \dfrac{r_2^2}{r^2}, & r_1 \le r \le r_2. \end{cases} \tag{59}$$

The associated stress components follow from the isotropic linear elastic constitutive relations,

$$\sigma_{rr} = 2\mu_i\,\varepsilon_{rr} + \lambda_i\left(\varepsilon_{rr} + \varepsilon_{\theta\theta}\right), \tag{60}$$

and

$$\sigma_{\theta\theta} = 2\mu_i\,\varepsilon_{\theta\theta} + \lambda_i\left(\varepsilon_{rr} + \varepsilon_{\theta\theta}\right). \tag{61}$$

The material interface is described implicitly by the level-set function $\varphi(x, y) = \sqrt{x^2 + y^2} - r_1$.

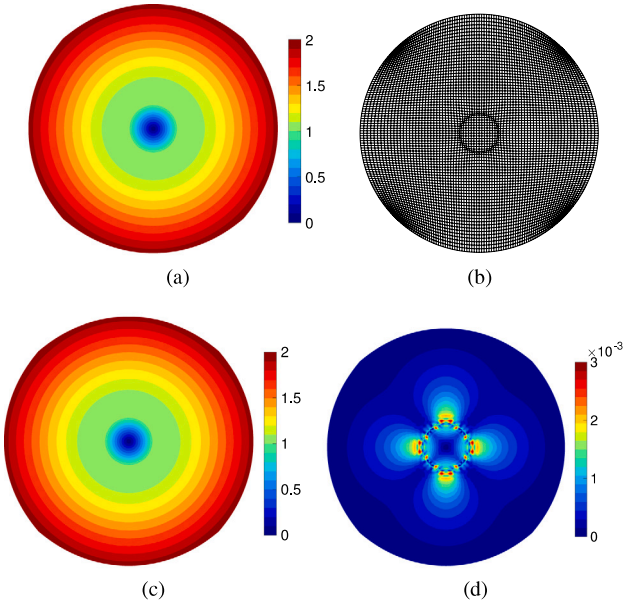

Fig. 7. Radial displacement field for the circular inclusion benchmark: (a) analytical reference solution, (b) r-adapted spline parameterization of the geometry, (c) numerical solution computed with the proposed method, and (d) absolute error distribution $|u_r^h - u_r^{\text{ex}}|$.

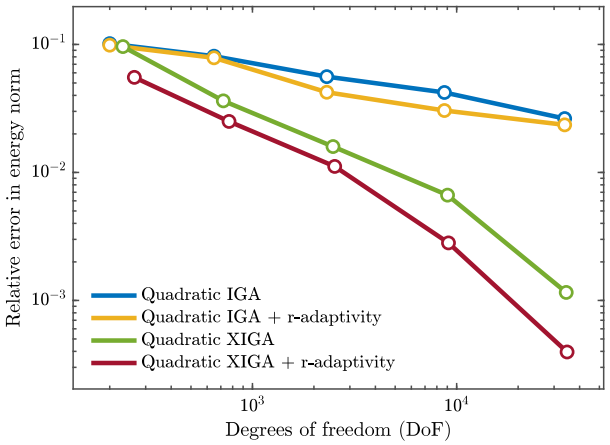

Fig. 8. Convergence behavior for the circular inclusion benchmark: relative error in the energy norm versus the number of degrees of freedom for IGA, XIGA, and the proposed method.

Fig. 7 illustrates the effect of the proposed r-adaptive strategy. The adapted parameterization in Fig. 7(b) concentrates iso-parameter lines near the material interface, leading to a numerical displacement field (Fig. 7(c)) that closely matches the analytical reference solution. The discrepancy between the two solutions is confined to a thin band around the interface, as shown in the error map in Fig. 7(d). This demonstrates that the control-point relocation increases resolution locally while preserving the spline space and the number of degrees of freedom.

Fig. 8 shows the convergence behavior in the energy norm. For a fixed number of degrees of freedom, the r-adaptive discretizations consistently produce smaller errors than the corresponding non-adaptive formulations, with the r-adaptive XIGA achieving the highest accuracy. Although enrichment improves the approximation space, the results reveal that a substantial portion of the error is associated with insufficient geometric resolution of the material interface. The redistribution

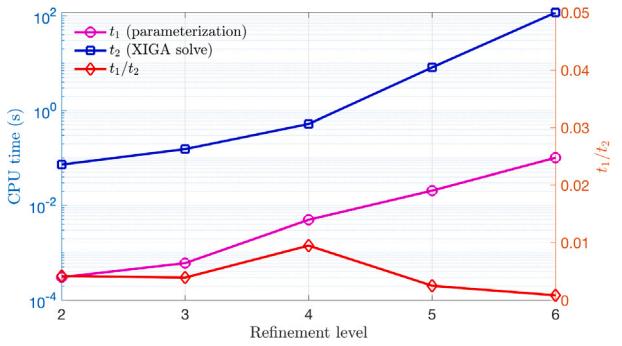

Fig. 9. Computational cost versus refinement level for the bi-material inclusion benchmark. The r-adaptive parameterization time t_1 and XIGA solution time t_2 are shown on a logarithmic scale (left axis), together with their ratio t_1/t_2 (right axis). The geometric adaptation stage represents only a small fraction of the total runtime across all refinement levels.

of control points reduces this geometric error component, enabling the enriched approximation to attain its expected accuracy. Overall, the results demonstrate that r-adaptivity improves accuracy without increasing the number of degrees of freedom, yielding a more efficient discretization for weak-discontinuous problems.

Fig. 9 compares the CPU time of the geometry parameterization stage with that of solving the enriched XIGA system. Both costs increase with refinement, but the additional overhead introduced by the r-adaptive relocation remains minor. Across all tested discretizations, the ratio t_1/t_2 stays below 1%, indicating that geometric adaptation is inexpensive relative to the solution procedure. Therefore, the proposed r-adaptive strategy enhances accuracy while adding only negligible computational overhead, in contrast to nonlinear optimization-based r-adaptive approaches that typically incur substantial additional cost [13, 25].

5.1.2. *Influence of the density-function parameters*

The monitor function defined in Eq. (47) involves three user-defined parameters that control the local distribution of control points. The peak value of ρ at the interface is $\rho_0 + \alpha$, while the far-field value is ρ_0, so the peak-to-background ratio is

$$\frac{\rho_{\text{peak}}}{\rho_{\text{bg}}} = 1 + \frac{\alpha}{\rho_0}. \tag{62}$$

The ratio α/ρ_0 therefore governs the contrast of the parameterization, while δ determines the width of the refinement band along the interface. To clarify the role of each parameter and to establish recommended ranges, we conduct two complementary studies on a benchmark configuration consisting of a circular inclusion in a circular plate. For each parameter, we examine both the resulting parameterization and the accuracy of the corresponding IGA solution.

Effect of the ratio α/ρ_0. The bandwidth is fixed at $\delta = 0.1$, which produces a sufficiently narrow peak for the interface-induced refinement to be clearly distinguishable from the background. Three representative values of ρ_0 are considered while keeping $\alpha = 1.25$ fixed, corresponding to ratios $\alpha/\rho_0 \in \{12.5, 1.25, 0.125\}$.

Fig. 10 shows the resulting parameterizations. For the largest ratio (Fig. 10(a)), control points concentrate aggressively along the interface, producing a sharply localized refinement region surrounded by an essentially uniform far-field mesh. The interface resolution is highest, at the cost of coarsening the bulk. For an intermediate ratio (Fig. 10(b)), the refinement region remains clearly visible but is wider and transitions smoothly into the surrounding mesh, providing a balanced trade-off between interface and bulk resolution. When the ratio drops well below unity (Fig. 10(c)), the interface-induced peak is dwarfed by

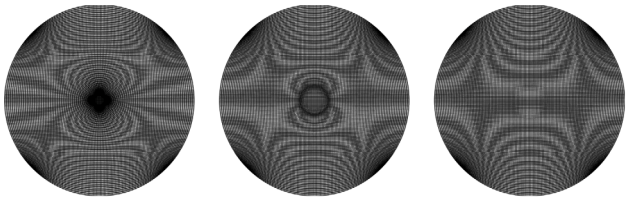

(a) $\rho_0 = 0.1$, $\alpha/\rho_0 = 12.5$ (b) $\rho_0 = 1$, $\alpha/\rho_0 = 1.25$ (c) $\rho_0 = 10$, $\alpha/\rho_0 = 0.125$

Fig. 10. Influence of the peak-to-background ratio α/ρ_0 on the adapted spline parameterization, for fixed $\alpha = 1.25$ and $\delta = 0.1$. (a) $\rho_0 = 0.1$: aggressive interface concentration; (b) $\rho_0 = 1$: balanced refinement; (c) $\rho_0 = 10$: peak suppressed, adaptation effectively deactivated.

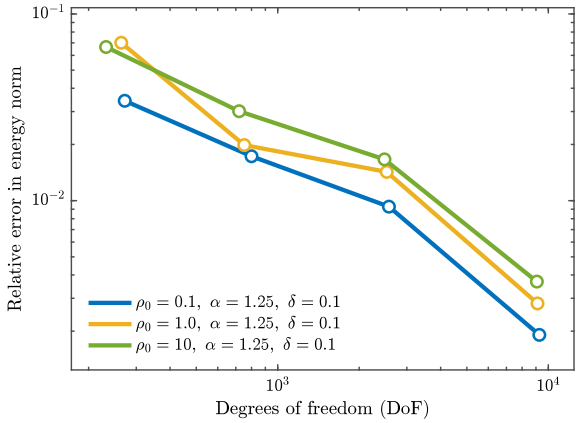

Fig. 11. Convergence of the relative error in the energy norm for the three configurations of Fig. 10 ($\alpha = 1.25$ and $\delta = 0.1$ fixed). All configurations attain the same asymptotic convergence rate, while the error level decreases monotonically as α/ρ_0 increases.

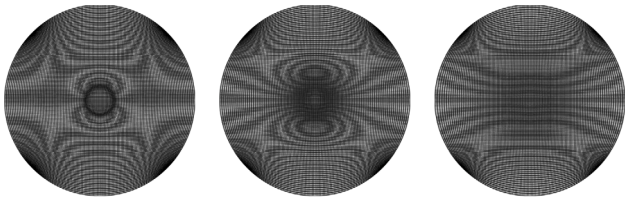

(a) $\delta = 0.1$ (b) $\delta = 0.5$ (c) $\delta = 1.0$

Fig. 12. Influence of the bandwidth parameter δ on the adapted spline parameterization, for fixed $\rho_0 = 1$ and $\alpha = 1.25$. (a) narrow refinement band tightly localized along the interface; (b) wider band with a smooth transition into the bulk; (c) influence region covering most of the domain.

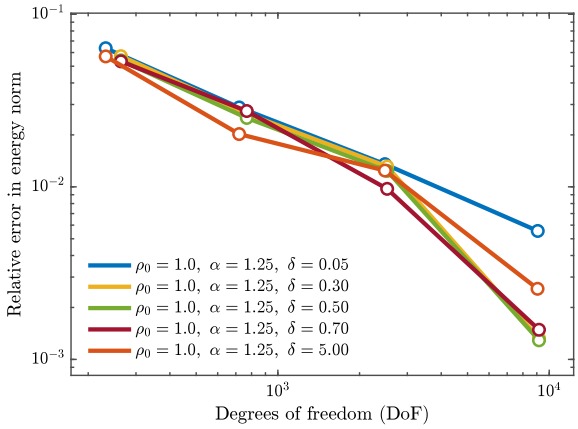

Fig. 13. Convergence of the relative error in the energy norm for four representative values of δ, with $\rho_0 = 1$ and $\alpha = 1.25$ held fixed. The two intermediate values ($\delta = 0.3$ and $\delta = 0.7$) yield nearly identical errors, indicating that the method is insensitive to δ within this range; values outside it degrade either through a too-narrow band ($\delta = 0.05$) or a too-wide one ($\delta = 5$).

the background density, and the resulting parameterization is visually indistinguishable from a non-adapted mesh.

These visual differences translate directly into corresponding differences in solution accuracy. Fig. 11 reports the convergence of the relative error in the energy norm for the same three configurations. All curves attain a similar asymptotic convergence rate, consistent with the optimal rate of the underlying quadratic XIGA discretization, but the error level depends strongly on the ratio. The configuration with the largest ratio ($\alpha/\rho_0 = 12.5$) consistently yields the smallest error, while the deactivated configuration ($\alpha/\rho_0 = 0.125$) produces the largest error at every refinement level, with a gap of roughly half an order of magnitude. The intermediate ratio ($\alpha/\rho_0 = 1.25$) falls between these two extremes.

Effect of δ. We then fix $\rho_0 = 1$ and $\alpha = 1.25$ and vary δ to isolate its effect on the width of the refinement band. Note that δ does not affect the peak value $\rho_0+\alpha$ at the interface, but only the rate at which ρ decays toward ρ_0 away from it.

Fig. 12 illustrates the visual effect of δ on the parameterization. For $\delta = 0.1$ (Fig. 12(a)), the monitor function decays rapidly and the resulting refinement is tightly localized within a narrow band around the interface. Increasing δ to 0.5 (Fig. 12(b)) widens the refinement band and smooths its transition into the surrounding mesh: the same number of relocated control points is now distributed over a larger zone, so the local control-point density at the interface decreases. Further increasing δ to 1.0 (Fig. 12(c)) extends the influence region until it covers most of the domain.

To assess the impact of these visual differences on solution accuracy, δ is varied over more than two orders of magnitude with the same ρ_0 and α. Fig. 13 reports the resulting convergence curves for four representative values. The curves split into three regimes. For $\delta \in [0.3, 1]$, the curves are nearly indistinguishable, indicating that the method is essentially insensitive to δ within this range. Outside this range, the error degrades noticeably: a too-narrow band ($\delta = 0.05$) fails to cover the physical transition zone of the strain field, with the error increasing by approximately one order of magnitude at the finest discretization, while a too-wide band ($\delta = 5$) extends across most of the domain and loses the contrast in control-point density, recovering the behavior of a non-adaptive parameterization. The bandwidth δ therefore admits a robust intermediate range, outside of which the adaptation becomes ineffective.

Recommended parameter ranges. Based on the present study, parameter combinations with $\alpha/\rho_0 \in [1, 20]$ and $\delta \in [0.3, 0.7]$ produce parameterizations in which control points are clearly concentrated along the interface while preserving sufficient resolution in the bulk, yielding the smallest IGA errors at comparable numbers of degrees of freedom. The settings used in the numerical examples of this paper ($\alpha/\rho_0 = 1.25$ and $\delta = 0.5$) lie within this recommended range. Within this range, the method does not require fine tuning of the parameters, which supports the practical robustness of the proposed formulation.

5.2. Plate with four circular inclusions

This example investigates the performance of the proposed adaptive XIGA formulation in the presence of multiple material interfaces. Compared to the single-inclusion benchmark, the coexistence of several

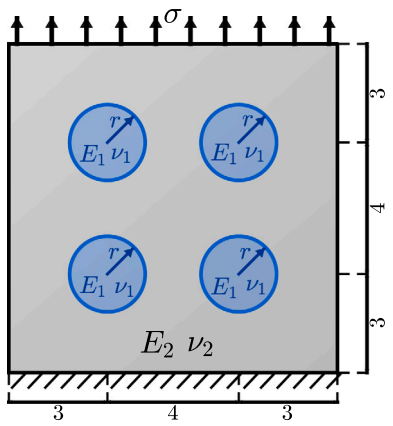

Fig. 14. Four-inclusion bi-material benchmark. A square plate contains four circular inclusions embedded in a matrix. A uniform tensile traction is applied on the top boundary and the bottom boundary is fixed.

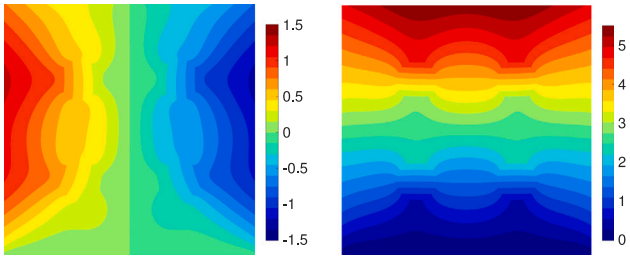

Fig. 15. Contour plots of the computed displacement components obtained with the adaptive r-refined parameterization: (a) horizontal displacement u_x and (b) vertical displacement u_y.

interfaces introduces competing resolution requirements, providing a more demanding test for the geometry-driven adaptation strategy.

A square plate of side length $L = 10$ containing four circular inclusions is considered, see Fig. 14. Each inclusion has radius $r = 0.8$. Plane strain conditions are assumed. The material parameters are $(E_1, \nu_1) = (1, 0.25)$ and $(E_2, \nu_2) = (10, 0.3)$. A uniformly distributed tensile traction $\sigma = 5$ is applied on the top boundary, while the bottom edge is fully fixed.

The four interfaces are circular inclusions with common radius $r = 0.8$ and centers $\mathbf{c}_1 = (-2, -2)$, $\mathbf{c}_2 = (-2, 2)$, $\mathbf{c}_3 = (2, -2)$, and $\mathbf{c}_4 = (2, 2)$. The corresponding level-set functions are defined as signed distance functions $\varphi^{(k)}(\mathbf{x}) = \|\mathbf{x} - \mathbf{c}_k\| - r$, where $k = 1, 2, 3, 4$.

Fig. 16(a) shows the adapted spline parameterization, where control points concentrate along the inclusion boundaries due to the stress gradients jump induced by material contrast.

As a consequence, the displacement field in Fig. 15 remains smooth within each material subdomain while preserving weak discontinuities across the interfaces. The corresponding stress components in Fig. 16 exhibit localized variations along the inclusion boundaries, indicating that the interface behavior is properly resolved without increasing the number of basis functions.

The stress components σ_{xx}, σ_{yy}, and σ_{xy} shown in Figs. 16(b)–16(d) exhibit localized concentrations around the inclusion boundaries. No oscillatory patterns appear in the vicinity of the material interfaces, suggesting that the adaptive parameterization improves interface resolution while maintaining numerical stability.

Fig. 17 shows the convergence behavior for the four-inclusion problem. All discretizations exhibit a monotonic error decay under refinement. However, for comparable numbers of degrees of freedom, the r-adaptive formulations consistently achieve smaller errors than the corresponding non-adaptive ones.

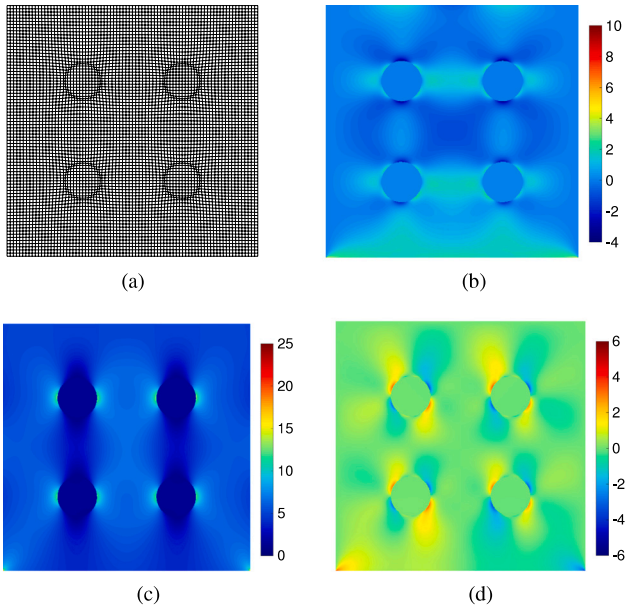

Fig. 16. r-adapted spline parameterization and resulting stress fields for the four-inclusion bi-material problem: (a) adapted spline parameterization; (b) σ_{xx}; (c) σ_{yy}; and (d) σ_{xy}.

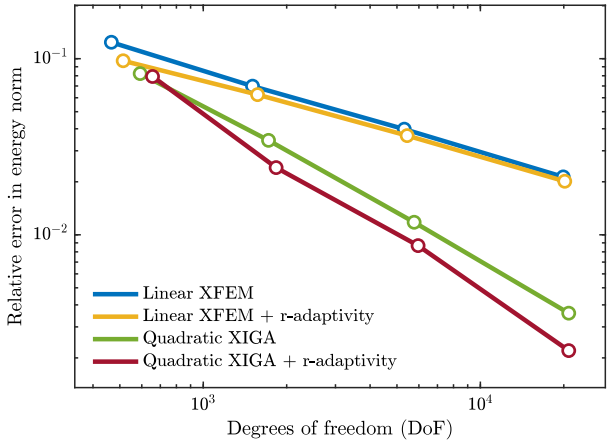

Fig. 17. Log–log convergence behavior for the plate with four circular inclusions. The relative error in the energy norm is plotted against the number of degrees of freedom (DoFs) for linear and quadratic XIGA formulations, with and without r-adaptivity.

The improvement is observed for both linear XFEM and quadratic XIGA approximations, with the quadratic r-adaptive XIGA attaining the highest accuracy. This indicates that, in the presence of multiple interfaces, a significant portion of the discretization error originates from insufficient geometric resolution. By redistributing control points among competing interfaces, the proposed strategy reduces this geometric error component and allows the enriched approximation to reach its expected accuracy.

Fig. 18 compares the computational cost of the geometry parameterization and the extended IGA solution. Both costs grow with refinement due to the increasing number of degrees of freedom, yet the overhead introduced by the r-adaptive relocation remains small. Across all refinement levels, the ratio t_1/t_2 stays below 1%, indicating that the geometric adaptation does not dominate the computational effort. Hence, even in the multi-interface setting, the proposed strategy improves accuracy without introducing a significant additional computational burden.

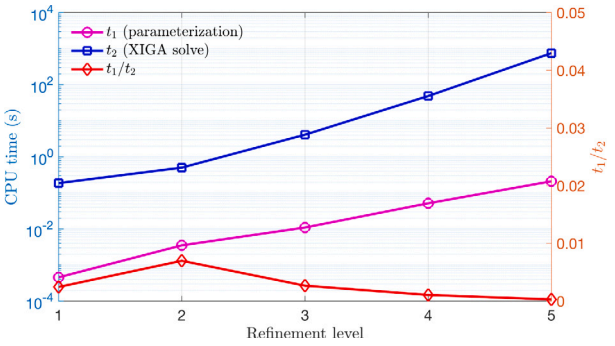

Fig. 18. Computational cost versus refinement level ($\rho_0/\alpha = 1/1.25$, $\delta = 1$). Parameterization time t_1 and solution time t_2 are shown on a logarithmic scale, together with their ratio t_1/t_2.

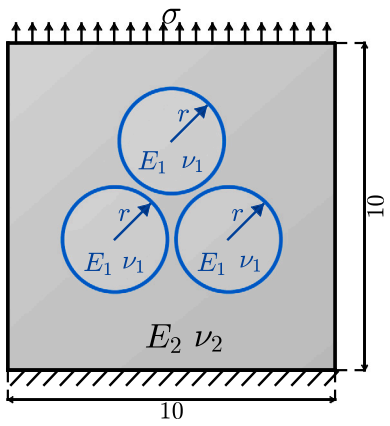

Fig. 19. Three closely spaced inclusion benchmark. The small separation distance leads to strongly interacting strain fields.

5.3. Plate with three closely spaced circular inclusions

This example examines the most challenging configuration considered in this study, where multiple material interfaces are located in close proximity. In contrast to the previous multi-inclusion benchmark, the distance between interfaces becomes comparable to the element size, causing overlapping enrichment supports and strongly interacting strain fields. This setting provides a stringent test of whether the proposed r-adaptivity can distribute the resolution among neighboring discontinuities.

The physical domain is a square plate of side length $L = 10$ containing three identical circular inclusions of radius $r = 1.6$, see Fig. 19. The inclusion centers are $\mathbf{c}_1 = (0, 2)$, $\mathbf{c}_2 = (-\sqrt{3}, -1)$, and $\mathbf{c}_3 = (\sqrt{3}, -1)$. Material parameters are $(E_1, \nu_1) = (1, 0.25)$ and $(E_2, \nu_2) = (10, 0.3)$. The bottom boundary is fully constrained and a uniform vertical traction $\sigma = 1$ is applied on the top edge.

The interfaces are described by signed-distance level-set functions $\varphi^{(k)}(\mathbf{x}) = \|\mathbf{x} - \mathbf{c}_k\| - r$, where $k = 1, 2, 3$.

Due to the small separation distance between the inclusions, their strain fields strongly interact, creating competing resolution requirements in a confined region. This configuration therefore constitutes a stringent test for the adaptive redistribution of control points near neighboring interfaces.

Fig. 21(a) shows the adapted spline parameterization. Control points concentrate in the narrow regions between neighboring inclusions, where overlapping strain gradients arise due to the small interface separation.

As a consequence, the displacement field in Fig. 20 remains smooth within each material subdomain while preserving weak discontinuities

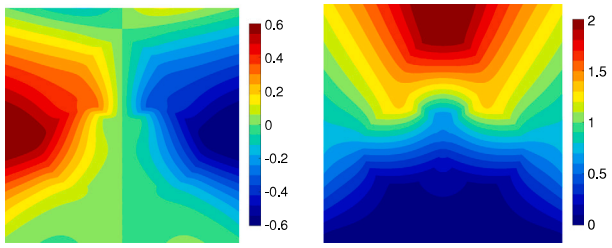

Fig. 20. Contour plots of the computed displacement components obtained with the adaptive r-refined parameterization: (a) horizontal displacement u_x and (b) vertical displacement u_y.

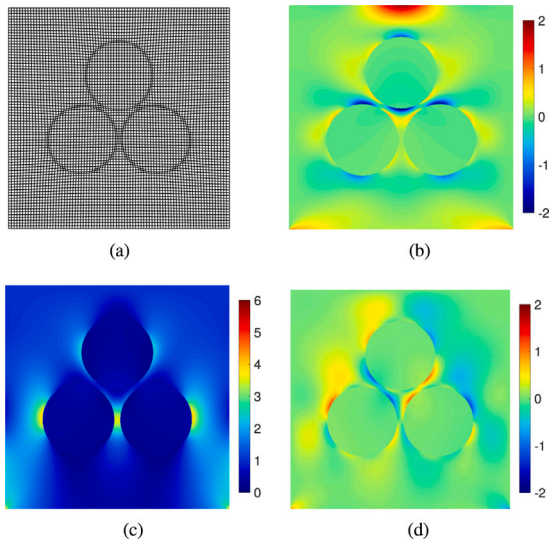

Fig. 21. r-adapted spline parameterization and resulting stress fields for the three-inclusion bi-material problem: (a) adapted spline parameterization; (b) σ_{xx}; (c) σ_{yy}; and (d) σ_{xy}, showing strong gradients resolved along the inclusion boundaries.

across all interfaces. The stress components in Figs. 21(b)–21(d) exhibit sharply localized transitions along the inclusion boundaries without oscillatory patterns.

These results indicate that the adaptive relocation distributes geometric resolution among closely spaced interfaces, maintaining stability while resolving the interface response without increasing the number of degrees of freedom.

Fig. 22 shows the convergence behavior for the plate with three closely spaced inclusions. All discretizations converge under refinement; however, the non-adaptive formulations retain noticeably larger errors at comparable numbers of degrees of freedom.

The benefit of the r-adaptive parameterization becomes more pronounced than in the previous example. When interfaces are close, insufficient geometric resolution produces persistent approximation errors. By redistributing control points within the narrow regions separating the inclusions, the proposed strategy significantly reduces this error component.

As a result, both linear XFEM and quadratic XIGA approximations achieve lower errors, with the quadratic r-adaptive XIGA attaining the highest accuracy. This demonstrates that geometry-driven relocation restores the expected convergence behavior without increasing the number of basis functions.

5.4. Bi-material plate with a heart-shaped inclusion

In contrast to the previous benchmarks, which involved smooth circular interfaces, this example examines a non-trivial, non-circular

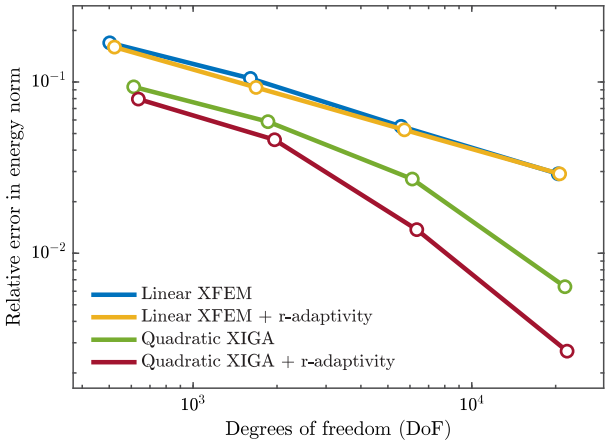

Fig. 22. Log–log convergence behavior for the plate with three closely spaced inclusions. Relative energy-norm error versus number of degrees of freedom for linear XFEM and quadratic XIGA formulations, with and without *r*-adaptivity.

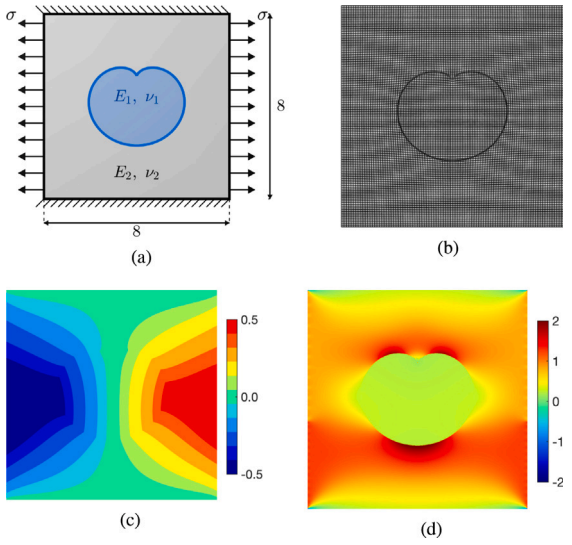

Fig. 23. Bi-material plate with a heart-shaped inclusion under uniaxial tension: (a) problem setup, showing the 8×8 matrix domain (E_2, ν_2) containing a heart-shaped inclusion (E_1, ν_1), with the top and bottom edges fixed in the vertical direction and a uniform traction σ applied on the lateral edges; (b) *r*-adapted spline parameterization, with control points clustered along the inclusion interface to resolve the geometric curvature and the non-smooth cusp; (c) horizontal displacement field u_x; and (d) normal stress component σ_{xx}, showing the strong gradient accurately captured across the inclusion interface.

interface that is non-convex and contains a geometric singularity in the form of a cusp. Such features generate locally concentrated strain gradients that cannot be resolved by uniform refinement alone, and therefore provide a stringent test of whether the proposed *r*-adaptivity can redistribute control points toward both the smoothly curved portions and the non-smooth apex of the interface.

The physical domain is a square plate of side length $L = 8$ containing a single heart-shaped inclusion centered at the origin, see Fig. 23(a). Plane strain conditions are assumed. The material parameters are $(E_1, \nu_1) = (1, 0.25)$ for the inclusion and $(E_2, \nu_2) = (10, 0.3)$ for the matrix. The top and bottom edges are vertically constrained, while a uniform horizontal traction $\sigma = 1$ is applied on the lateral edges. The interface is described by a level-set function consistent with the notation introduced earlier. Working in the rescaled coordinates

$$\tilde{x} = \frac{x}{\lambda s}, \qquad \tilde{y} = \frac{y - y_0}{s}, \tag{63}$$

the cardioid interface is the zero set of

$$\varphi(\mathbf{x}) = \tilde{x}^2 + \tilde{y}^2 + \tilde{y} - \sqrt{\tilde{x}^2 + \tilde{y}^2}, \tag{64}$$

with $\varphi < 0$ inside the inclusion and $\varphi > 0$ in the matrix. Here $s = 1.5$ is a shape factor of the cardioid (distinct from the plate side length L), $\lambda = 1.06$ is a horizontal stretching factor, and y_0 is chosen so that the inclusion is centered in the matrix. The cusp arises at $\theta = \pi/2$, where the curve admits two distinct one-sided tangents, embedding a localized non-smooth feature within an otherwise smooth interface.

Fig. 23(b) shows the adapted spline parameterization. Control points concentrate along the curved portions of the interface and additionally cluster near the cusp, where the tangent discontinuity induces a localized strain concentration. In contrast to the smooth circular benchmarks, the redistribution along the interface is markedly non-uniform: the local density of control points adapts to the local geometric features without manual intervention.

As a consequence, the displacement field in Fig. 23(c) remains smooth within each material subdomain while preserving the weak discontinuity across the interface. The stress component σ_{xx} in Fig. 23(d) exhibits a sharp transition along the inclusion boundary and a pronounced concentration at the cusp, both resolved without spurious oscillations. For brevity, only u_x and σ_{xx} are reported here, as these are the components most directly aligned with the loading direction; u_y, σ_{yy}, and σ_{xy} exhibit analogous behavior.

Fig. 24 shows the convergence behavior for the heart-shaped inclusion problem. All discretizations exhibit a monotonic error decay under refinement; however, the *r*-adaptive formulations consistently attain smaller errors than the corresponding non-adaptive ones at

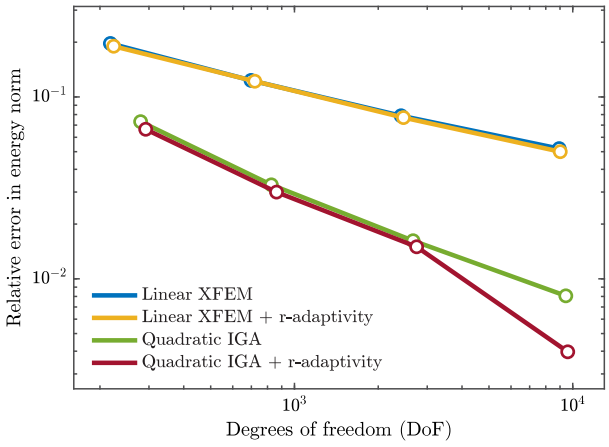

Fig. 24. Log–log convergence behavior for the plate with a heart-shaped inclusion. Relative energy-norm error versus number of degrees of freedom for linear XFEM and quadratic XIGA formulations, with and without *r*-adaptivity.

comparable numbers of degrees of freedom. The improvement is most pronounced for the quadratic *r*-adaptive XIGA, which benefits most from the geometry-driven relocation when the interface contains a non-smooth feature. This indicates that, in the presence of a geometric singularity, a significant portion of the discretization error originates from insufficient resolution of the singular feature itself. By redistributing control points toward the cusp, the proposed strategy reduces this geometric error component and allows the enriched approximation to recover its expected convergence rate.

Fig. 25 compares the computational cost of the geometry parameterization and the extended IGA solution. Both costs grow with refinement due to the increasing number of degrees of freedom, yet the overhead introduced by the *r*-adaptive relocation remains small. Across all refinement levels, the ratio t_1/t_2 stays below 1%, indicating that the geometric adaptation does not dominate the computational effort.

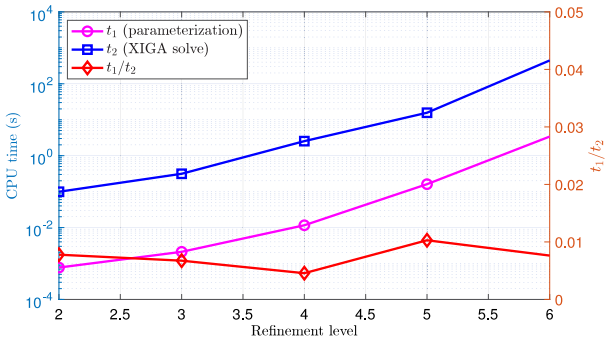

Fig. 25. Computational cost versus refinement level ($\alpha/\rho_0 = 1.275$, $\delta = 0.5$). Parameterization time t_1 and solution time t_2 are shown on a logarithmic scale, together with their ratio t_1/t_2.

Hence, even when the interface contains a non-smooth feature, the proposed strategy improves accuracy without introducing a significant additional computational burden.

6. Conclusion and outlook

This work proposed an extended *r*-adaptive isogeometric framework for problems with weak discontinuities in solution derivatives. By coupling enrichment with a level-set-based monitor function, the method redistributes control points according to interface geometry instead of refinement-based resolution, thereby enhancing accuracy near material interfaces while preserving the spline topology and maintaining a fixed number of degrees of freedom. Numerical experiments show consistent error reduction and recovery of the expected convergence behavior across different discretizations, including linear extended finite element method and quadratic extended isogeometric analysis. The improvement is particularly pronounced for multiple or closely spaced interfaces, where geometric resolution becomes the dominant source of discretization error. Moreover, the parameterization stage represents only a small fraction of the total runtime, indicating that the accuracy gain is obtained without a noticeable computational overhead.

Future work will focus on three directions. First, the extension to three-dimensional problems and CAD-derived geometries will assess applicability to realistic engineering configurations. Second, combining the present *r*-adaptivity with enrichment or continuity-reduction techniques may enable the treatment of strong discontinuities. Third, the development of rigorous a posteriori error estimators and automatic parameter selection for the monitor function will allow fully automated adaptive simulations.

CRediT authorship contribution statement

Jingyi Cao: Writing – original draft, Visualization, Validation, Software, Conceptualization. **Ye Ji:** Conceptualization, Formal analysis, Methodology, Software, Supervision, Writing – original draft, Visualization, Writing – review & editing. **Matthias Möller:** Conceptualization, Funding acquisition, Writing – review & editing, Supervision, Methodology. **Chungang Zhu:** Conceptualization, Methodology, Supervision, Validation, Writing – review & editing, Funding acquisition, Investigation.

Declaration of competing interest

The authors declare that they have no known competing financial interests or personal relationships that could have appeared to influence the work reported in this paper.

Acknowledgments

The authors would like to thank the anonymous reviewers for their valuable comments and suggestions. This work was partially supported by the National Natural Science Foundation of China (Grant No. 12471358).

Data availability

Data will be made available on request.

References

[1] LeVeque RJ, Li Z. The immersed interface method for elliptic equations with discontinuous coefficients and singular sources. SIAM J Numer Anal 1994;31(4):1019–44.
[2] Melenk JM, Babuška I. The partition of unity finite element method: basic theory and applications. Comput Methods Appl Mech Engrg 1996;139(1–4):289–314.
[3] Belytschko T, Black T. Elastic crack growth in finite elements with minimal remeshing. Internat J Numer Methods Engrg 1999;45(5):601–20.
[4] Moës N, Dolbow J, Belytschko T. A finite element method for crack growth without remeshing. Internat J Numer Methods Engrg 1999;46(1):131–50.
[5] Hughes TJ, Cottrell JA, Bazilevs Y. Isogeometric analysis: CAD, finite elements, NURBS, exact geometry and mesh refinement. Comput Methods Appl Mech Engrg 2005;194(39–41):4135–95.
[6] Cottrell JA, Hughes TJ, Bazilevs Y. Isogeometric analysis: Toward integration of CAD and FEA. John Wiley & Sons; 2009.
[7] The Constructor. Prestressed concrete: Principles, advantages, and applications. 2026, URL: https://theconstructor.org/concrete/prestressed-concrete-principles-advantages/28/. (Accessed 09 February 2026).
[8] Wikipedia contributors. Dental implant — Wikipedia, the free encyclopedia. 2026, URL: https://en.wikipedia.org/wiki/Dental_implant. (Accessed 09 February 2026).
[9] Ghorashi SS, Valizadeh N, Mohammadi S. Extended isogeometric analysis for simulation of stationary and propagating cracks. Internat J Numer Methods Engrg 2012;89(9):1069–101.
[10] Nguyen VP, Bordas S. Extended isogeometric analysis for strong and weak discontinuities. In: Isogeometric methods for numerical simulation. Springer; 2015, p. 21–120.
[11] Hu W, Zhang J, Li X. Higher order stable generalized isogeometric analysis for interface problems. J Comput Appl Math 2024;444:115792.
[12] Huang W, Russell RD. In: Adaptive moving mesh methods, vol. 174, Springer Science & Business Media; 2010.
[13] Ji Y, Wang MY, Wang Y, Zhu CG. Curvature-based r-adaptive planar NURBS parameterization method for isogeometric analysis using bi-level approach. Computer-Aided Des 2022;150:103305.
[14] Zhang J, Deng Q, Li X. A generalized isogeometric analysis of elliptic eigenvalue and source problems with an interface. J Comput Appl Math 2022;407:114053.
[15] Bahari M, Mantzaflaris A. Simultaneous rh-adaptive isogeometric analysis using optimal transport and THB-splines for gradient-dominated problems. Computer-Aided Des 2026;104105. http://dx.doi.org/10.1016/j.cad.2026.104105.
[16] Piegl L, Tiller W. The NURBS book. Springer Science & Business Media; 2012.
[17] Ji Y, Chen K, Möller M, Vuik C. On an improved PDE-based elliptic parameterization method for isogeometric analysis using preconditioned Anderson acceleration. Comput Aided Geom Design 2023;102:102191.
[18] Moës N, Cloirec M, Cartraud P, Remacle JF. A computational approach to handle complex microstructure geometries. Comput Methods Appl Mech Engrg 2003;192(28–30):3163–77.
[19] Osher S, Sethian JA. Fronts propagating with curvature-dependent speed: Algorithms based on Hamilton-Jacobi formulations. J Comput Phys 1988;79(1):12–49.
[20] Tran A, Yvonnet J, He QC, Toulemonde C, Sanahuja J. A multiple level set approach to prevent numerical artefacts in complex microstructures with nearby inclusions within XFEM. Internat J Numer Methods Engrg 2011;85(11):1436–59.
[21] Hou W, Jiang K, Zhu X, Shen Y, Li Y, Zhang X, Hu P. Extended Isogeometric Analysis with strong imposing essential boundary conditions for weak discontinuous problems using B++ splines. Comput Methods Appl Mech Engrg 2020;370:113135.
[22] Zienkiewicz OC, Zhu JZ. The superconvergent patch recovery and a posteriori error estimates. Part 1: The recovery technique. Internat J Numer Methods Engrg 1992;33(7):1331–64.

[23] Yu T, Bui TQ. Numerical simulation of 2-D weak and strong discontinuities by a novel approach based on XFEM with local mesh refinement. Comput Struct 2018;196:112–33.

[24] Gu J, Yu T, Nguyen TT, Tanaka S, Bui TQ, et al. Multi-inclusions modeling by adaptive XIGA based on LR B-splines and multiple level sets. Finite Elem Anal Des 2018;148:48–66.

[25] Ji Y, Wang M, Yu Y, Zhu C. Curvature-based r-adaptive isogeometric analysis with injectivity-preserving multi-sided domain parameterization. J Syst Sci Complex 2023;36(1):53–76.

[26] Sukumar N, Chopp DL, Moës N, Belytschko T. Modeling holes and inclusions by level sets in the extended finite-element method. Comput Methods Appl Mech Engrg 2001;190(46–47):6183–200.